Tissue-like phantoms for quantitative birefringence imaging

Liu, Xinyu; Beaudette, Kathy; Wang, Xianghong; Liu, Linbo; Bouma, Brett E.; Villiger, Martin

2017

Liu, X., Beaudette, K., Wang, X., Liu, L., Bouma, B. E., & Villiger, M. (2017). Tissue-like phantoms for quantitative birefringence imaging. Biomedical Optics Express, 8(10), 4454-4465.

https://hdl.handle.net/10356/87063

https://doi.org/10.1364/BOE.8.004454

Research Article | Vol. 8, No. 10 | 1 Oct 2017 | BIOMEDICAL OPTICS EXPRESS 4454
Biomedical Optics EXPRESS

Tissue-like phantoms for quantitative birefringence imaging

XINYU LIU,[1] KATHY BEAUDETTE,[2,3] XIANGHONG WANG,[1] LINBO LIU,[1,4] BRETT E. BOUMA,[3,5] AND MARTIN VILLIGER[3,*]

[1]*School of Electrical & Electronic Engineering, Nanyang Technological University, 50 Nanyang Avenue, 639798, Singapore*
[2]*Polytechnique Montréal, Department of Engineering Physics, P.O. Box 6079 Station Centre-Ville, Montréal, Québec H3C 3A7, Canada*
[3]*Wellman Center for Photomedicine, Harvard Medical School and Massachusetts General Hospital, 40 Blossom Street, Boston, MA 02114, USA*
[4]*School of Chemical and Biomedical Engineering, Nanyang Technological University, 62 Nanyang Dr, 637459, Singapore*
[5]*Institute for Medical Engineering and Science, Massachusetts Institute of Technology, Cambridge, MA 02139, USA*
**mvilliger@partners.org*

Abstract: Birefringence imaging, including polarization sensitive optical coherence tomography (PS-OCT), can provide valuable insight into the microscopic structure and organization of many biological tissues. In this paper, we report on a method to fabricate tissue-like birefringence phantoms for such imaging modalities. We utilize the photo-elastic effect, wherein birefringence is induced by stretching a polymer sample after heating it above its glass-transition temperature. The cooled samples stably exhibit homogeneous birefringence, and were assembled into phantoms containing multiple well-defined regions of distinct birefringence. We present planar slab phantoms for microscopy applications and cylindrical phantoms for catheter-based imaging and demonstrate quantitative analysis of the birefringence within individual regions of interest. Birefringence phantoms enable testing, validating, calibrating, and improving PS-OCT acquisition systems and reconstruction strategies.

OCIS codes: (170.4500) Optical coherence tomography; (110.5405) Polarimetric imaging; (170.3010) Image reconstruction techniques; (170.3880) Medical and biological imaging.

References and links

1. G. Lamouche, B. F. Kennedy, K. M. Kennedy, C.-E. Bisaillon, A. Curatolo, G. Campbell, V. Pazos, and D. D. Sampson, "Review of tissue simulating phantoms with controllable optical, mechanical and structural properties for use in optical coherence tomography," Biomed. Opt. Express **3**(6), 1381–1398 (2012).
2. A. Agrawal, T. J. Pfefer, N. Gilani, and R. Drezek, "Three-dimensional characterization of optical coherence tomography point spread functions with a nanoparticle-embedded phantom," Opt. Lett. **35**(13), 2269–2271 (2010).
3. X. Liu, S. Chen, D. Cui, X. Yu, and L. Liu, "Spectral estimation optical coherence tomography for axial super-resolution," Opt. Express **23**(20), 26521–26532 (2015).
4. A. Curatolo, B. F. Kennedy, and D. D. Sampson, "Structured three-dimensional optical phantom for optical coherence tomography," Opt. Express **19**(20), 19480–19485 (2011).
5. M. Strupler, A. M. Beckley, F. Benboujja, S. Dubois, I. Noiseux, O. Mermut, J. P. Bouchard, and C. Boudoux, "Toward an automated method for optical coherence tomography characterization," J. Biomed. Opt. **20**(12), 126007 (2015).
6. C.-É. Bisaillon and G. Lamouche, "Artery phantoms for intravascular optical coherence tomography: diseased arteries," J. Biomed. Opt. **18**, 096010 (2013).
7. J. Baxi, W. Calhoun, Y. J. Sepah, D. X. Hammer, I. Ilev, T. J. Pfefer, Q. D. Nguyen, and A. Agrawal, "Retina-simulating phantom for optical coherence tomography," J. Biomed. Opt. **19**(2), 021106 (2013).
8. M. R. Hee, D. Huang, E. Swanson, and J. G. Fujimoto, "Polarization-sensitive low-coherence reflectometer for birefringence characterization and ranging," J. Opt. Soc. Am. B **9**(6), 903 (1992).
9. J. F. de Boer, T. E. Milner, M. J. van Gemert, and J. S. Nelson, "Two-dimensional birefringence imaging in biological tissue by polarization-sensitive optical coherence tomography," Opt. Lett. **22**(12), 934–936 (1997).

#302382 https://doi.org/10.1364/BOE.8.004454
Journal © 2017 Received 19 Jul 2017; revised 27 Aug 2017; accepted 29 Aug 2017; published 12 Sep 2017

Biomedical Optics EXPRESS

10. C. E. Saxer, J. F. de Boer, B. H. Park, Y. Zhao, Z. Chen, and J. S. Nelson, "High-speed fiber based polarization-sensitive optical coherence tomography of in vivo human skin," Opt. Lett. **25**(18), 1355–1357 (2000).
11. W. Y. Oh, S. H. Yun, B. J. Vakoc, M. Shishkov, A. E. Desjardins, B. H. Park, J. F. de Boer, G. J. Tearney, and B. E. Bouma, "High-speed polarization sensitive optical frequency domain imaging with frequency multiplexing," Opt. Express **16**(2), 1096–1103 (2008).
12. Y. Lim, Y.-J. Hong, L. Duan, M. Yamanari, and Y. Yasuno, "Passive component based multifunctional Jones matrix swept source optical coherence tomography for Doppler and polarization imaging," Opt. Lett. **37**(11), 1958–1960 (2012).
13. W. Y. Oh, B. J. Vakoc, S. H. Yun, G. J. Tearney, and B. E. Bouma, "Single-detector polarization-sensitive optical frequency domain imaging using high-speed intra A-line polarization modulation," Opt. Lett. **33**(12), 1330–1332 (2008).
14. B. Park, M. Pierce, B. Cense, and J. de Boer, "Real-time multi-functional optical coherence tomography," Opt. Express **11**(7), 782–793 (2003).
15. E. Götzinger, M. Pircher, W. Geitzenauer, C. Ahlers, B. Baumann, S. Michels, U. Schmidt-Erfurth, and C. K. Hitzenberger, "Retinal pigment epithelium segmentation by polarization sensitive optical coherence tomography," Opt. Express **16**(21), 16410–16422 (2008).
16. N. Lippok, M. Villiger, and B. E. Bouma, "Degree of polarization (uniformity) and depolarization index: unambiguous depolarization contrast for optical coherence tomography," Opt. Lett. **40**(17), 3954–3957 (2015).
17. C. Fan and G. Yao, "Imaging myocardial fiber orientation using polarization sensitive optical coherence tomography," Biomed. Opt. Express **4**(3), 460–465 (2013).
18. J. F. de Boer, C. K. Hitzenberger, and Y. Yasuno, "Polarization sensitive optical coherence tomography - a review [Invited]," Biomed. Opt. Express **8**(3), 1838–1873 (2017).
19. B. Baumann, "Polarization sensitive optical coherence tomography: a review of technology and applications," Appl. Sci. **7**(5), 474 (2017).
20. S. Fukuda, G. Kishino, S. Hoshi, S. Beheregaray, Y. Ueno, M. Fukuda, D. Kasaragod, Y. Yasuno, and T. Oshika, "Repeatability of corneal phase retardation measurements by polarization-sensitive optical coherence tomography," Invest. Ophthalmol. Vis. Sci. **56**(5), 3196–3201 (2015).
21. R. G. Sayegh, S. Zotter, P. K. Roberts, M. M. Kandula, S. Sacu, D. P. Kreil, B. Baumann, M. Pircher, C. K. Hitzenberger, and U. Schmidt-Erfurth, "Polarization-sensitive optical coherence tomography and conventional retinal imaging strategies in assessing foveal integrity in geographic atrophy," Invest. Ophthalmol. Vis. Sci. **56**(9), 5246–5255 (2015).
22. K. H. Kim, M. C. Pierce, G. Maguluri, B. H. Park, S. J. Yoon, M. Lydon, R. Sheridan, and J. F. de Boer, "In vivo imaging of human burn injuries with polarization-sensitive optical coherence tomography," J. Biomed. Opt. **17**(6), 066012 (2012).
23. W. C. Y. Lo, M. Villiger, A. Golberg, G. F. Broelsch, S. Khan, C. G. Lian, W. G. Austen, Jr., M. Yarmush, and B. E. Bouma, "Longitudinal, 3D imaging of collagen remodeling in murine hypertrophic scars in vivo using polarization-sensitive optical frequency domain imaging," J. Invest. Dermatol. **136**(1), 84–92 (2016).
24. D. C. Adams, L. P. Hariri, A. J. Miller, Y. Wang, J. L. Cho, M. Villiger, J. A. Holz, M. V. Szabari, D. L. Hamilos, R. Scott Harris, J. W. Griffith, B. E. Bouma, A. D. Luster, B. D. Medoff, and M. J. Suter, "Birefringence microscopy platform for assessing airway smooth muscle structure and function in vivo," Sci. Transl. Med. **8**(359), 359ra131 (2016).
25. J. N. van der Sijde, A. Karanasos, M. Villiger, B. E. Bouma, and E. Regar, "First-in-man assessment of plaque rupture by polarization-sensitive optical frequency domain imaging in vivo," Eur. Heart J. **37**(24), 1932 (2016).
26. F. A. South, E. J. Chaney, M. Marjanovic, S. G. Adie, and S. A. Boppart, "Differentiation of ex vivo human breast tissue using polarization-sensitive optical coherence tomography," Biomed. Opt. Express **5**(10), 3417–3426 (2014).
27. M. Villiger, D. Lorenser, R. A. McLaughlin, B. C. Quirk, R. W. Kirk, B. E. Bouma, and D. D. Sampson, "Deep tissue volume imaging of birefringence through fibre-optic needle probes for the delineation of breast tumour," Sci. Rep. **6**(1), 28771 (2016).
28. Z. Ding, C.-P. Liang, Q. Tang, and Y. Chen, "Quantitative single-mode fiber based PS-OCT with single input polarization state using Mueller matrix," Biomed. Opt. Express **6**(5), 1828–1843 (2015).
29. C. Hitzenberger, E. Goetzinger, M. Sticker, M. Pircher, and A. Fercher, "Measurement and imaging of birefringence and optic axis orientation by phase resolved polarization sensitive optical coherence tomography," Opt. Express **9**(13), 780–790 (2001).
30. C. Fan and G. Yao, "Mapping local retardance in birefringent samples using polarization sensitive optical coherence tomography," Opt. Lett. **37**(9), 1415–1417 (2012).
31. M. Villiger, E. Z. Zhang, S. Nadkarni, W. Y. Oh, B. E. Bouma, and B. J. Vakoc, "Artifacts in polarization-sensitive optical coherence tomography caused by polarization mode dispersion," Opt. Lett. **38**(6), 923–925 (2013).
32. M. Villiger, E. Z. Zhang, S. K. Nadkarni, W. Y. Oh, B. J. Vakoc, and B. E. Bouma, "Spectral binning for mitigation of polarization mode dispersion artifacts in catheter-based optical frequency domain imaging," Opt. Express **21**(14), 16353–16369 (2013).
33. S. Makita, M. Yamanari, and Y. Yasuno, "Generalized Jones matrix optical coherence tomography: performance and local birefringence imaging," Opt. Express **18**(2), 854–876 (2010).

Biomedical Optics EXPRESS

34. P. H. Mott and C. M. Roland, "Elasticity of Natural Rubber Networks," Macromolecules **29**(21), 6941–6945 (1996).
35. "Elastomer Polyisoprene (natural rubber)," http://www.substech.com/dokuwiki/doku.php?id=elastomer_polyisoprene_natural_rubber
36. "Polycarbonate," http://www.polymerprocessing.com/polymers/PC.html.
37. B. W. Pogue and M. S. Patterson, "Review of tissue simulating phantoms for optical spectroscopy, imaging and dosimetry," J. Biomed. Opt. **11**, 041102 (2006).
38. S. K. Nadkarni, M. C. Pierce, B. H. Park, J. F. de Boer, P. Whittaker, B. E. Bouma, J. E. Bressner, E. Halpern, S. L. Houser, and G. J. Tearney, "Measurement of collagen and smooth muscle cell content in atherosclerotic plaques using polarization-sensitive optical coherence tomography," J. Am. Coll. Cardiol. **49**(13), 1474–1481 (2007).
39. M. C. Pierce, R. L. Sheridan, B. Hyle Park, B. Cense, and J. F. de Boer, "Collagen denaturation can be quantified in burned human skin using polarization-sensitive optical coherence tomography," Burns **30**(6), 511–517 (2004).
40. S. Alali, A. Gribble, and I. A. Vitkin, "Rapid wide-field Mueller matrix polarimetry imaging based on four photoelastic modulators with no moving parts," Opt. Lett. **41**(5), 1038–1041 (2016).

1. Introduction

Resolution test targets and tissue-mimicking phantoms are essential to test, optimize, calibrate, and evaluate optical imaging systems [1]. The USAF 1951 resolution test target is frequently used to test an imaging system's lateral resolution. In optical coherence tomography (OCT), the axial resolution often exceeds the resolution in the lateral direction, and the axial point spread function (PSF) can be readily measured from a reflecting surface. To directly assess the three dimensional PSF, targets containing point-like scatterers, such as laser marks or beads embedded in a transparent matrix can be used [2,3]. Beyond characterization of the PSF, to evaluate the structural and functional imaging performance, phantoms that mimic the optical, structural, and possibly mechanical properties of real biological tissue are highly valuable [1]. Curatolo *et al*. demonstrated an OCT phantom using lithographic casting to produce three-dimensional structures embedded in a silicone matrix [4]. Strupler *et al.* used a diamond-turned aluminum multi-segment mirror covered by a tissue-mimicking material along with a calibration algorithm to determine volumetric field-of-view, axial resolution, and image curvature [5]. Bisaillon *et al*. discussed different strategies to create phantoms of coronary arteries [6]. To test imaging performance and software segmentation accuracy, Baxi *et al.* developed a phantom precisely replicating retinal morphology [7].

An important extension of conventional OCT is polarization sensitive OCT (PS-OCT) [8,9] which employs polarization-diverse detection to measure the polarization state of light backscattered by the sample. To make the measurements tolerant to layered samples with varying polarization properties, many PS-OCT systems probe the sample with two input polarization states, either sequentially on successive A-lines using a polarization modulator [10], simultaneously by multiplexing in frequency [11,12], or by rapidly varying the polarization state within individual A-lines [13]. PS-OCT complements the conventional backscatter intensity images with additional contrast, such as retardation [14], degree of polarization (DOP) [15,16], and optic axis orientation [17]. Birefringence corresponds to the difference of the refractive indices ($\Delta n = n_e - n_o$) experienced by light prepared along the extraordinary (n_e) and the ordinary (n_o) polarization states, respectively. In a uniaxial material without diattenuation, these two principle states are orthogonal to each other. Retardation, δ, denotes the phase delay accrued over a distance L between light polarized along each of the two principle states, and is related to the birefringence by $\delta = 2\pi\Delta nL/\lambda$, with λ the central wavelength of the light. In biological tissues, birefringence occurs mostly in regularly arranged fibrillary tissues, such as collagen, muscle, or myelin. Accordingly, PS-OCT, recently reviewed by de Boer *et al* [18]. and Baumann [19], has attracted attention for imaging a range of samples, including the cornea [20], retina [21], skin burns [22] and scars [23], airway smooth muscle [24], coronary atherosclerosis [25], and breast tumor [26,27].

Biomedical Optics EXPRESS

Over time, an array of different PS-OCT implementations and reconstruction methods has been developed. For their validation, wave plates [28] and biological tissues, such as muscle [29] or tendon [30], are frequently used as test samples. Although a wave plate is stable and well-controlled, its specular reflections are a poor approximation of the backscattering properties of biological tissues and do not necessarily reveal the shortcomings of a PS-OCT imaging system [31]. Muscle and tendon generate the typical speckle signal of biological tissue and exhibit birefringence. However, their nominal amount and distribution of birefringence are unknown, and they are perishable, precluding repeated and controlled assessment and cross-validation of PS-OCT imaging systems.

We previously have used rubber phantoms for PS-OCT [16,32]. By stretching the rubber sample to different lengths, we could control the amount of stress-induced birefringence and the optic axis orientation. However, controlling the applied stress and holding the sample in the stretched position proved to be challenging and complicated the assembly of phantoms containing regions with distinct birefringence levels. Furthermore, for un-vulcanized stretched rubber samples, we observed significant birefringence decay within just a few hours due to stress relaxation, impeding attempts to produce stable phantoms with well-defined amounts of birefringence.

In this paper, we describe a method to fabricate robust and durable phantoms containing spatially defined elements of predetermined birefringence and optic axis orientation. We developed an approach to induce a controlled amount of stable birefringence in polycarbonate films, overcoming the drawbacks encountered with the rubber. We present phantoms comprising multiple elements of distinct birefringence in two layers with different optic axis orientation, tailored for either galvanometer-based or catheter-based PS-OCT imaging. We performed depth-resolved birefringence imaging of the phantoms using our implementation of PS-OCT [32] and analyzed the birefringence of the different elements.

2. Methods

2.1 PS-OCT imaging

Throughout this work, we used a polarization-modulated, fiber-based optical frequency domain imaging (OFDI) setup, similar to the one described in [32]. In short, the system employed a wavelength-swept laser source centered at 1300 nm, with a tuning range of 115 nm, leading to an axial resolution of < 10 μm in tissue, and a repetition rate of 103.6 kHz. An acousto-optic modulator (AOM) was inserted in the reference arm for resolving depth degeneracy. The polarization of the light in the sample arm was modulated with an electro-optic modulator between linear and circular polarization states in adjacent A-lines, before directing the light through a circulator to either a benchtop unit, composed of two galvanometric mirrors and a scan lens (LSM03, Thorlabs), or a motor drive unit (Terumo) interfaced with commercial intravascular catheters (FastView, Terumo).

Recorded data were processed with spectral binning [32] to obtain maps of depth-resolved birefringence and DOP. We used one-fifth of the original spectral bandwidth (i.e., nine overlapping spectral bins), a lateral Gaussian filter having a full width at half maximum equal to 12 adjacent A-lines, and an axial offset of 48 μm to derive birefringence. A reduction of the DOP indicates a randomization of the detected polarization states within a small neighborhood around each pixel. This depolarization can serve as an independent contrast mechanism [15], but strong depolarization also precludes the reconstruction of meaningful birefringence. We used DOP to validate the reliability of the reconstructed birefringence. Birefringence and DOP are displayed using a near isoluminant color map, overlaid with the intensity tomogram [32].

Biomedical Optics EXPRESS

2.2 Phantom design

For birefringence imaging with PS-OCT, an ideal phantom should 1) exhibit sufficient back-scattering to generate an appreciable OCT signal; 2) contain several laterally and axially well-defined regions with distinct, but homogeneous birefringence; 3) have a non-birefringent scattering host matrix. The scattering properties of both the birefringent elements and the background matrix should result in a fully-developed speckle pattern in the reconstructed tomogram to best mimic biological tissues. The spatial confinement of the birefringent elements enables segmentation and evaluation of the accuracy of birefringence measurement within these areas.

For single input state PS-OCT, which reconstructs cumulative retardation and assumes a constant orientation of the optic axis along depth, a single birefringent layer would be sufficient. Recently, increased effort has been directed to reconstructing local retardation (i.e. birefringence) [33], offering a more intuitive view of tissues having a layered architecture. Furthermore, the optic axis orientation can also be reconstructed in a depth-resolved manner [17]. To accommodate these capabilities, we aimed for two axially superposed birefringent layers with distinct optic axis orientations, as shown schematically in Fig. 1. One layer is a long birefringent band, and the other consists of four birefringent elements with distinct birefringence levels. The angle of the optic axes between the two birefringent layers is maximized at 45 degrees. The birefringent elements are embedded into a non-birefringent matrix and offer a convenient geometry for benchtop imaging. To also enable catheter-based PS-OCT imaging, we integrated a similar arrangement of birefringent elements into the background matrix coated along a glass capillary tube.

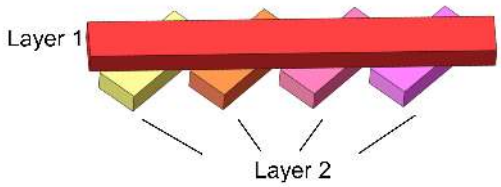

Fig. 1. Birefringent elements arrangement in the phantom. Layer 1 consists of a long birefringent band; Layer 2 consists of four birefringent elements with distinct birefringence levels.

2.3 Stress-induced birefringence

Stress induces birefringence in many polymers by increasing the alignment of the polymer chains, an effect known as photo-elasticity. The birefringence Δn across a band of photo-elastic material is linearly correlated to the stress σ [34]:

$$\Delta n = C\sigma, \tag{1}$$

where C is known as the stress optical coefficient. Further, the stress is linearly related to the strain for an elastic material. We have previously used the elasticity of rubber latex to conveniently generate controlled amounts of birefringence. However, for un-vulcanized rubber samples, we observed a slow but significant decay of the induced birefringence continuing for hours and days. We attribute this to the two competitive effects that are taking place in a stretched rubbery material, as illustrated in Fig. 2(a). The first effect is elastic deformation, which increases the alignment of the polymer chains, thereby creating birefringence; the second is viscous flow, whereby molecule chains slide against each other and decrease the birefringence. This second effect leads to the so-called “stress relaxation” in viscoelastic materials.

Biomedical Optics EXPRESS

The rubbery state of polymers is an intermediate phase between the glassy solid state and the liquid phase, as summarized in Fig. 2(b). The temperature separating the glassy state from the rubbery state is the glass-transition temperature. Un-vulcanized rubber (polyisoprene, glass-transition temperature of –70 °C [35]) resides in the rubbery phase at room temperature and exhibits the typical viscoelastic properties of this state.

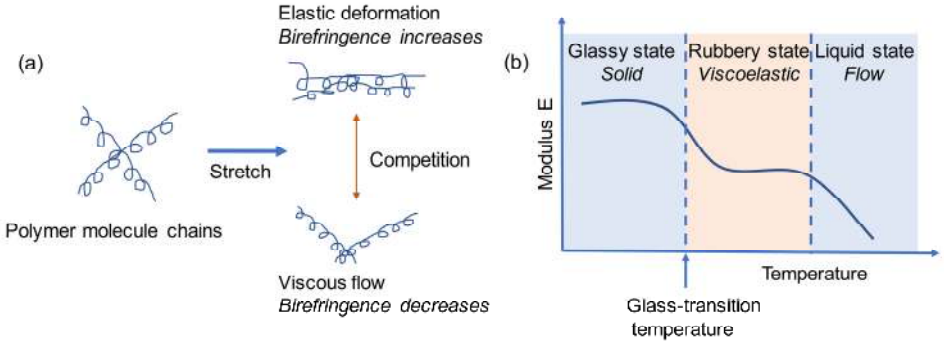

Fig. 2. (a) Behavior of polymer chains of rubbery state polymers under tension. (b) Physical state transitions in polymers as a function of temperature.

To overcome the shortcomings of the rubber's viscoelasticity, we opted for a polymer with a higher glass-transition temperature, i.e. above room temperature. We chose polycarbonate (PC), which has a glass-transition temperature of 145°C [36]. Both scattering and transparent PC films are commercially available with various thickness options. Here, we used films with a thickness of 250 µm (CT301326, Goodfellow Inc). Scattering PC films generate a suitable OCT signal with fully-developed speckle and are easy to cut to desired dimensions using scissors or a paper trimmer. Heating PC above 145°C and converting it to the viscoelastic state enables controlled stretching without necessitating significant force. Cooling the stretched material and returning it to the glassy state 'freezes' the molecular arrangement and maintains the induced birefringence, but releases the contracting force induced by the elastic deformation.

2.4 Annealing

The manufacturing process of PC films appears to induce residual stress that results in a birefringence pattern visible in cross-sectional images (Fig. 3(a)). To create samples with homogeneous and controllable birefringence and optic axis orientation, the residual birefringence should be removed before stretching. Taking advantage of the stress relaxation phenomenon, we cut the PC film into 10-mm wide strips, sandwiched them between two metal plates, and put them into an oven at 150°C for 24 hours of annealing. This process completely removes the residual birefringence stress and provides samples with homogeneously low birefringence at baseline (Fig. 3(b)). The metal plates are necessary to prevent the PC film from buckling, and strips annealed better than larger sheets, presumably because they release internal stress also through in-plane bending.

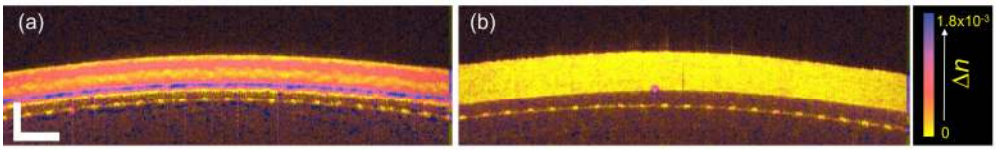

Fig. 3. PS-OCT cross-sections showing (a) birefringence patterns present in commercial PC films due to residual stress and (b) homogeneously low birefringence after annealing strips of PC. Horizontal and vertical scale bars: 2 mm and 250 µm, respectively.

Biomedical Optics EXPRESS

2.5 Stretching

The schematic of the setup used to stretch PC strips, along with the detailed procedure, is shown in Fig. 4(a). We used weights (2 × ~200g) secured directly to the PC strip to apply a constant traction force. Rails were used to avoid swinging of the weights. To apply stress to the PC strip only after the transition to the rubbery state, we placed the entire stretching setup in the oven at 150°C, while supporting the weights with a spacer. After heating for 30 minutes, the spacer was removed to apply the stress, which elongated the strip. The amount of elongation was controlled by the height of the spacer. Once the weights reached their lower position, we immediately opened the oven door to cool down the PC sample and removed the entire setup from the oven.

The stress, σ, is defined by the force of gravity pulling down the weights, G, and the cross-sectional area of the strip, A, and is given by $\sigma = G/A$. Once the weights reach their lower position, the support balances the forces to maintain the stress corresponding to this elongation. To obtain birefringence comparable in magnitude to that of most biological tissues (i.e. 0 to ~2×10^{-3}), a strain of ~5% proved to be sufficient for PC. Therefore, the change of cross-sectional area during the stretching can be neglected, and the retardation δ can be controlled by adjusting the width w of the strip as:

$$\delta \propto 1/w. \tag{2}$$

In practice, it is challenging to accurately adjust the elongation to an absolute value. However, the width of each strip can be varied to generate different levels of birefringence while applying the same amount of elongation (Fig. 4(b)). The strips can then be cut into smaller elements suitable for integration into the final phantoms. Specifically, in our experiment, we prepared a series of PC strips with widths ranging from 2 to 7 mm. The original suspended length was 70 mm which was then stretched by 5% to 73.5 mm. The areas close to the ends (~10 mm) of the strips showed abnormal birefringence, and we only cut the middle part of the strips into bands (20 × 4 mm for slab and 10 × 2 mm for cylindrical phantoms) and smaller rectangular areas (2 × 4 mm for slab and 1 × 2 mm for cylindrical phantoms), and assembled them into phantoms. We also prepared small rectangular areas from annealed strips without stretching to serve as regions with lowest birefringence.

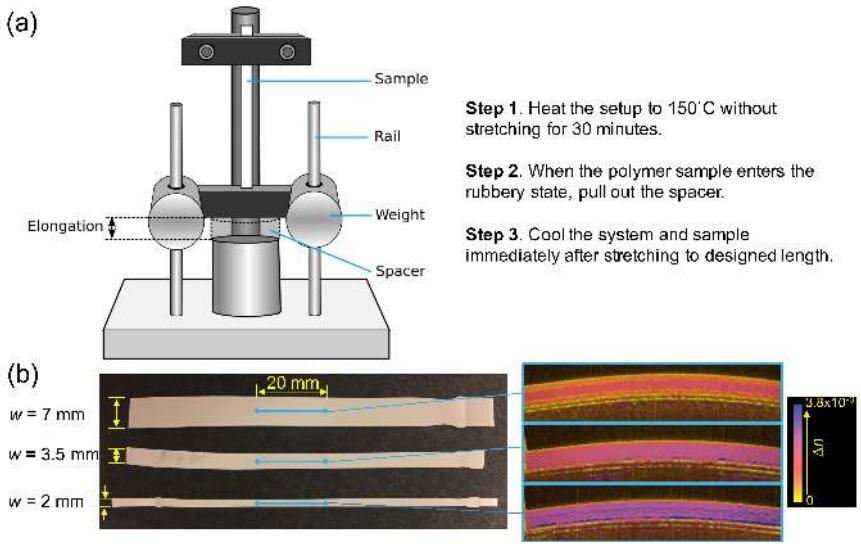

Fig. 4. (a) Schematic of the stretching apparatus and steps of pre-heating, stretching, and cooling. (b) Photograph of three PC strips of varying widths after stretching along with corresponding cross-sectional PS-OCT images showing the obtained birefringence levels.

Biomedical Optics EXPRESS

2.6 Matrix

Suitable candidate matrix materials for optical phantoms have been reviewed by Pogue *et al.* [37]. For our application, we chose epoxy (20-3440-032, Buehler Inc.), which is durable, transparent, and non-birefringent. More importantly, the epoxy resin is initially liquid and solidifies within 9 hours of curing after mixing with the epoxy hardener (20-3442-016, Buehler Inc.), allowing a convenient time window to cast the phantoms. Specifically, to make the matrix, we mixed 40 ml epoxy resin with 0.5 g TiO_2 powder (634662, Aldrich Inc.). To uniformly mix the particles into the epoxy, we ultrasonicated the mixture for 2 hours in a 60°C water bath. The hardener was then added to the resin at a volume ratio of 1:2, and poured into the mold. Molds were prepared from rubber latex (S25719, Fisher Science Education) to define the outer shape of the phantom. Rubber latex is frequently used to make molds, and is easy to separate from the cast after curing. The birefringent PC elements were placed and arranged within the mold as designed in Fig. 1 before pouring the epoxy. Slab phantoms were straightforward to cast, using an open rectangular mold. For cylindrical phantoms, we used glass capillaries (22-260-943, Fisher Scientific Inc.) as the innermost layer. The birefringent elements were glued to the outer surface of the capillary using epoxy. The capillary with the attached birefringent elements was then embedded in a cylindrical rubber mold and immersed in epoxy.

3. Results

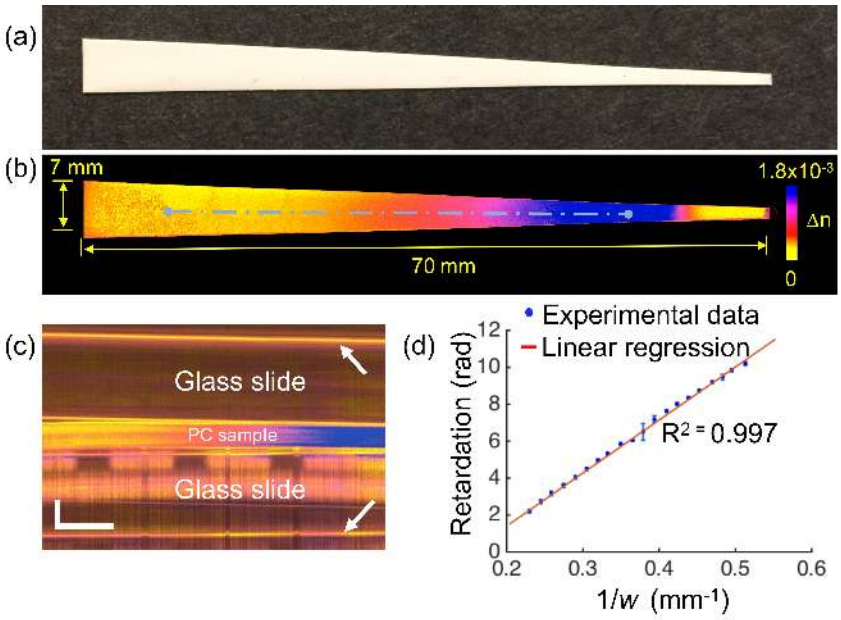

Fig. 5. (a) Photograph of the wedge sample after stretching and (b) matching en-face projection of birefringence obtained from volumetric PS-OCT data set. (c) A representative cross-sectional image illustrating the reference surfaces (arrows) used to measure the cumulative retardation. Horizontal and vertical scale bars: 1 mm and 250 μm, respectively. (d) Measured cumulative retardation against 1/*w*, where *w* is the width of the strip, along with linear regression. Error bars indicate the standard deviation across 20 measurements at distinct positions perpendicular to the wedge.

3.1 Birefringence measurement

To verify the relation between stress and induced birefringence, we prepared an annealed PC strip, cut it into a wedge shape, and stretched it using the proposed method to create birefringence, as shown in Fig. 5(a). Its linearly varying width is expected to result in an

Biomedical Optics EXPRESS

inversely related retardation. The resulting birefringence in the en-face projection, obtained by taking the mean birefringence between the manually segmented top and bottom surface of the wedge, indeed exhibits the expected behavior (Fig. 5(b)). However, reconstruction of the local retardation has its own limitations and potential artifacts, such as wrapping and increased dependence on speckle. To more directly assess the retardation of the light passing through the stretched wedge sample, we sandwiched the sample between two glass slides and determined the polarization state of the light reflected from the first surface of the top slide and the second surface of the bottom slide (Fig. 5(c)). To reduce the strong specular reflections and avoid detector saturation, the entire sample assembly was immersed in water for imaging. The two modulated input polarization states of our PS-OCT instrument allowed computation of the cumulative retardation between these two interfaces. Limiting the analysis to the central area along the strip (dot-dashed blue line in Fig. 5(b)), we unwrapped the retardation along the strip from the widest side of the strip, and evaluated the mean and the standard deviation of the retardation across 20 adjacent A-lines perpendicular to the wedge. We found a linear relation between $1/w$ and the mean retardation ($R^2 = 0.997$), as shown in Fig. 5(d). This confirms the expectation and demonstrates that the birefringence can be quantitatively controlled by adjusting the width of the strip.

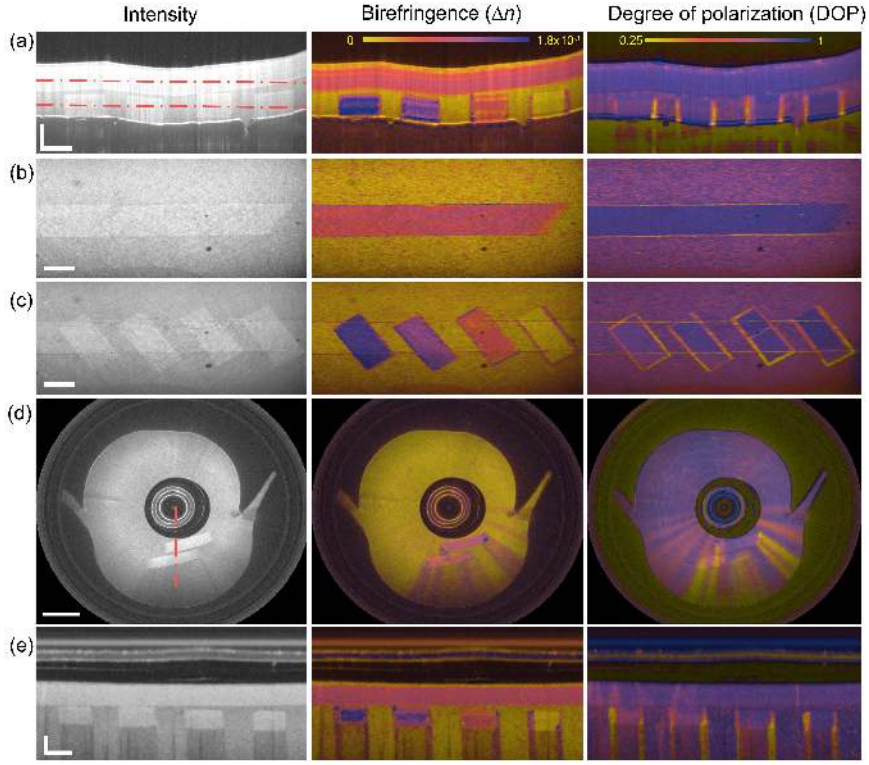

Fig. 6. Intensity, birefringence and DOP images of the slab (a-c) and cylindrical (d-e) phantoms. (a) Representative cross-sectional images of the birefringence phantom for galvanometer-scanning system. (b) & (c) En-face images at different depths as indicated by the dashed red lines in (a). Horizontal and vertical scale bars for (a-c): 2 mm and 250 µm, respectively. (d) Representative images obtained from one rotational scan with the catheter. Scale bar: 1 mm. (e) Longitudinal sections obtained from a pull-back data set, with its corresponding location indicated by the dashed red line in (d). Radial and horizontal scale bars: 250 µm and 1 mm, respectively.

Biomedical Optics EXPRESS

3.2 Assembled phantoms

Figure 6 presents intensity, birefringence and DOP images obtained from a slab (a-c) and cylindrical (d-e) phantom, respectively. For the slab phantom, Fig. 6(a) displays cross-sections through all the birefringent regions. Figures 6(b) and 6(c) are two en-face images, whose depth locations are indicated in Fig. 6(a). Figure 6(d) shows cross-sections of the cylindrical phantom imaged with a rotational scan of the side-looking fiber probe in the intravascular catheter. Figure 6(e) presents a corresponding longitudinal section generated from the volumetric data set recorded while rotating and pulling back the fiber probe.

Backscattering from the birefringent segments is slightly stronger than from the matrix, and already delineates the individual elements. The birefringence maps present more clearly the individual elements and their varying birefringence levels. The DOP indicates uniform polarization states, except at the vertical edges of the embedded segments. Although the refractive indices of the PC strips and the matrix material appear very close, it is likely their residual difference that perturbs the polarization states in these areas. This effect is more pronounced in catheter-based imaging, where the probing beam propagates through this interface, not merely along it as in case of benchtop imaging. Nevertheless, within the birefringent elements, the DOP remains high, validating the reconstructed measures of birefringence.

3.3 Phantom analysis

The clear spatial definition of the homogeneously birefringent elements enables convenient quantitative analysis of these regions. Using the slab phantom, we manually segmented three-dimensional regions of interest by identifying the corners of each birefringent element. Figures 7(a) and 7(b) display volume renderings of the elements and their segmentations. For each segment, the histogram of the measured birefringence was computed. Results for all regions are displayed in Fig. 7(c). The mean of measured birefringence values in each segmentation is regarded as the nominal Δn of each element. To confirm the stability of the induced birefringence, we imaged the same phantom after three months and repeated the analysis. As shown in Fig. 7(d), we found close agreement between the two measurements, and concluded that the phantom was stable over this long period.

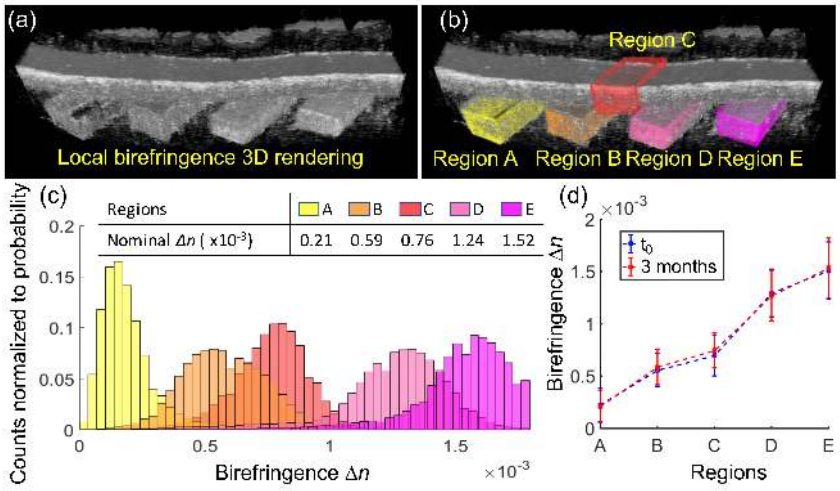

Fig. 7. (a) & (b) Volume rendering of the slab phantom along with the segmentation of the individual birefringent elements. (c) Histogram of the birefringence measurements for each segmented region. (d) Mean Δn and standard deviations for the initial and the repeat measurement after 3 months.

Biomedical Optics EXPRESS

4. Discussion

Reconstruction of cumulative retardation or birefringence in PS-OCT is subject to many system and processing-dependent artifacts. The birefringence phantoms that we fabricated generate a tissue-like backscattering signal and contain spatially confined areas with a homogeneous, predictable amount of birefringence, in a range comparable to the birefringence reported in biological tissues such as muscle and collagen [38,39]. These phantoms can help to benchmark different PS-OCT architectures and reconstruction strategies. Segmentation of the individual elements facilitates quantitative analysis and enables comparison of imaging systems. The stability of the phantoms even allows comparing systems that are in separate locations, and could enable calibration of birefringence measurements.

Although we put great effort into generating homogeneously birefringent elements, it is likely that a residual variation within the strips remains, which may be more appreciable with higher-resolution PS-OCT. The unique capability of PS-OCT to measure polarization signatures from scattering media makes it challenging to independently validate the generated levels of birefringence. The scattering properties of the utilized PC films exclude polarized light microscopy. Transparent PC films feature a different stress optical coefficient. And cutting thin slices of the material may induce additional stress that alters the observed birefringence. Whereas our current analysis focused on birefringence, these phantoms also enable assessing the reconstruction of the optic axis orientation. Similar phantoms could also be used for other implementations of tissue polarimetry, where stretched elastic materials have been used to induce birefringence [40].

We observed that the absolute amount of induced birefringence delicately depends on the detailed experimental conditions, such as the precise amount of elongation and temperature variations while handling the sample in the oven. At 150°C, the PC resides in a viscoelastic state with substantial viscosity. Stretching took a few to ten seconds, depending on the strip width. A perfectly elastic material would stretch immediately. Hence, the precise dynamics of the stretching and cooling process impact the resulting birefringence. Keeping all parameters constant by following the exact same steps and only varying the strip width allowed relative control of the birefringence. However, generating a sample with a predetermined absolute amount of birefringence would be challenging.

The PC material used in this study generates tissue-like scattering in the 1300-nm wavelength region. Preliminary imaging with a system operating at 800 nm suggested that the resulting backscattering may be too strong, compromising the typical OCT imaging depth. Acrylonitrile butadiene styrene (ABS) films (5751T, McMaster-Carr) offer an interesting alternative in this case. This ABS film is slightly more transparent, resulting in better imaging performance at 800 nm, and can be stretched above its glass-transition temperature (105 C°) in the same way that PC can be processed. In addition, we also noticed that in order to induce the same amount of birefringence, the required elongation for ABS is slightly larger than that of PC.

5. Summary

In this work, we presented a detailed protocol on the fabrication of tissue-like birefringence phantoms for the evaluation of PS-OCT instruments and algorithms. Although we use the photo-elastic effect, we induce birefringence after heating the sample above its glass-transition temperature. Returned to the glassy state at room temperature, the stretched material ceases to retract but maintains its birefringence level. The retardation and optic axis orientation can be accurately controlled. The reconstructed sample birefringence revealed clearly defined regions of distinct birefringence that enable a quantitative analysis. Our method for fabricating birefringence phantoms is simple, adaptable to arbitrary geometries, and does not require specialized skills. The resulting robust phantoms may prove valuable for the calibration, optimization, and evaluation of PS-OCT imaging systems.

Biomedical Optics EXPRESS

Funding

National Research Foundation Singapore (NRF-CRP13-2014-05); National Medical Research Council Singapore (NMRC/CBRG/0036/2013); Ministry of Education Singapore (MOE2013-T2-2-107); the NTU-AIT-MUV program in advanced biomedical imaging (NAM/15005); the National Institute of Biomedical Imaging and Bioengineering of the National Institutes of Health, award P41 EB015903, and by Terumo Corporation.

We acknowledge the valuable suggestions on polymer material processing from Dr. Kaiwei Li in Nanyang Technological University (Singapore).